In2S3 Growth Templated by Aluminogermanate Double-Walled Imogolite Nanotubes Toward Efficient Visible Light Photocatalysts

Sanjay Jatav, Hongxiao Xiang, Marcel Herber, Erwan Paineau, Eric H Hill

In_2S_3 Growth Templated by Ge-doped Double-Walled Imogolite Nanotubes towards Efficient Visible Light Photocatalysts

Sanjay Jatav, Hongxiao Xiang, Marcel Herber, Erwan Paineau, and Eric H. Hill**

S. Jatav, H. Xiang, M. Herber, E. H. Hill
Institute of Physical Chemistry, University of Hamburg, 20146 Hamburg, Germany
E-mail: eric.hill@chemie.uni-hamburg.de

E. Paineau
Université Paris-Saclay, CNRS, Laboratoire de Physique des Solides, 91405 Orsay, France
E-mail: erwan-nicolas.paineau@universite-paris-saclay.fr

Keywords: (clays, imogolite, In_2S_3, photocatalysis, water remediation, nanotubes)

Different strategies combining semiconductors and nanomaterials have been explored to enhance the performance of visible-light photocatalysts. This work reports the hydrothermal growth of In_2S_3 on the aluminogermanate double-walled imogolite nanotubes and the photocatalytic properties of the resulting composites. The reaction conditions are optimized to ensure the linear growth of In_2S_3, while preserving the tubular structure of imogolite nanotubes. The imogolite-In_2S_3 composites show enhanced photocatalytic degradation of methyl orange compared to the control In_2S_3, exhibiting a four-fold increase in the photocatalytic dye degradation rate constant. Interestingly, these composites present a negative photocurrent response, indicating the generation of mobile holes, whereas both In_2S_3 and imogolite by themselves exhibit the typical positive photocurrent behavior. The improvement in the photocatalytic dye degradation and the negative photocurrent response is attributed to the interface formation between In_2S_3 and imogolite in these composites and the p-type character of the latter. Templating the colloidal synthesis of semiconducting nanoparticles in confined spaces could bring a step-change in the design of catalytic and photocatalytic materials.

1. Introduction

Less energy intensive means for water decontamination are being sought due to increasing demand, dwindling fossil fuel reserves and problems associated with their use.[1,2] In this vein, solar means of decontaminating water are becoming attractive.[3,4] Indium sulfide, In_2S_3, is a III-V semiconductor which has been studied for its photocatalytic and photovoltaic properties.[5–7] Apart from possessing interesting optical properties, In_2S_3 is also appealing because of its low toxicity and stability under ambient settings.[8,9] One of the strategies for improving the performance of In_2S_3 is to combine it with other materials. For instance, composites with graphene,[10] ZnO[11] and MnS[12] have shown improvement in the photocatalytic performance over pristine In_2S_3. In a previous study we reported that in addition to conventional carbon-based materials (graphene, nanotubes), metal sulfides and oxides, layered silicate clays can also be used to enhance the photophysical properties of In_2S_3.[13] Such Laponite-In_2S_3 nanohybrids, comprised of thin layers of In_2S_3, showed an order of magnitude enhancement in photocurrent generation and photocatalytic efficiency compared to the In_2S_3 control. The possibility of templating In_2S_3 growth using a 1D template nanoparticle, and the resulting photocatalytic properties, led to the growth of In_2S_3 on aluminogermanate double walled imogolite nanotubes (GWINTs).

Imogolite is a clay nanotube with a general structural formula $(OH)_3Al_2O_3X(R)$ (with X = Si, Ge; R = OH, CH_3…), which appear as promising 1D templates.[14,15] INTs have the advantage to present a well-defined minimum in their strain energy,[16] resulting in nanotubes with monodisperse diameters.[17,18] In addition, the synthesis process is relatively straightforward, enabling to control the morphology (single. vs. double-walled structures, aspect ratio…) and the surface properties of the inner cavity by changing the nature of the precursors.[19–21] Thanks to their unique colloidal properties,[22] INTs have demonstrated their ability to effectively stabilize metal nanoparticles on their external surface[23–25] but, to date, the growth of semiconductor nanowires with INTs has not been truly explored.

Herein, the hydrothermal growth of In_2S_3 was performed in the presence of a colloidal dispersion of INT to obtain photocatalytic INT-In_2S_3 composites. By carefully controlling the reaction conditions, the tubular morphology of INT could be preserved and the In_2S_3 growth confined exclusively onto these tubes. These In_2S_3-decorated INT exhibited a four-fold enhancement in their photocatalytic dye degradation rate compared to the pristine In_2S_3, even though the former has a wider bandgap. In addition, the mechanism responsible for the

negative photocurrent response of the composite, which contrasts with the photocurrent response of the pristine INT and In_2S_3 control samples, has been proposed.

2. Materials and Methods

2.1. Chemicals

Tetraethoxygermane (TEOG), urea ($CO(NH_2)_2$), dodecyltrimethylammonium bromide (DTAB), thioacetamide (TAA), indium chloride ($InCl_3.5H_2O$) and methyl orange (MO) were purchased from Sigma-Aldrich Chemical Reagent Co., Ltd. Aluminum perchlorate nonahydrate ($Al(ClO_4)_3 \cdot 9H_2O$) and polyvinyl alcohol (PVA, molecular weight 88000- 97000 g/mol, 87-89% hydrolyzed) were procured from Alfa Aesar and Na_2SO_4 (>99%) was obtained from Chemsolute.

2.2. Synthesis

2.2.1 Ge-double-walled Imogolite nanotubes (GDWINT)

Aluminogermanate double-walled nanotubes were synthesized according to previously reported methods.[26]Typically, 50 mL of 0.2 M $Al(ClO_4)_3$ and 50 mL of 0.2 M $CO(NH_2)_2$ were mixed under stirring in a PFTE beaker. 1.11 mL of TEOG was added to obtain a molar ratio [Ge]:[Al]:[urea] = 1:2:2. The mixture was then transferred in an acid digestion bomb (Zeoclave, Maximator, France). The hydrothermal treatment was performed under autogenous pressure at 140°C for 5 days. After cooling down the autoclave, the resulting dispersion was dialyzed with ultra-pure water (resistivity 18 MΩ.cm) using semi-permeable membranes (Spectra/Por®, 10 kDa). The final solid concentration in GDWINT was determined by weight loss upon drying.

2.2.2. Hydrothermal In_2S_3 growth on INT

An aqueous dispersion of GDWINT (1.5 mL, 10 mg/mL) was added to 23.5 mL deionized water in a 50 mL Teflon beaker. Subsequently, DTAB (78 µL, 0.1M) was added to the above GDWINT dispersion under stirring. A previously prepared 5 mL solution of TAA (11 mg) and $InCl_3.5H_2O$ (5.43 mg) was added to the Teflon beaker and stirred for 5 mins. Then this beaker was sonicated for 5 mins and sealed in a hydrothermal autoclave (DAB-2, Berghof Instruments, Germany). The reaction was carried out at 180 °C for 1 hour, 3 hours and 5 hours. These samples are labelled as INT-IS_1h, INT-IS_3h and INT-IS_5h, respectively. An In_2S_3 control was prepared by using 50 times the amount of In and S precursor used for synthesizing the composites. The In_2S_3 control has been labelled as IS. All the above samples

were washed 5 times with water and 2 times with ethanol and then dried at 60 °C for 24 hours. The synthesis scheme is shown below.

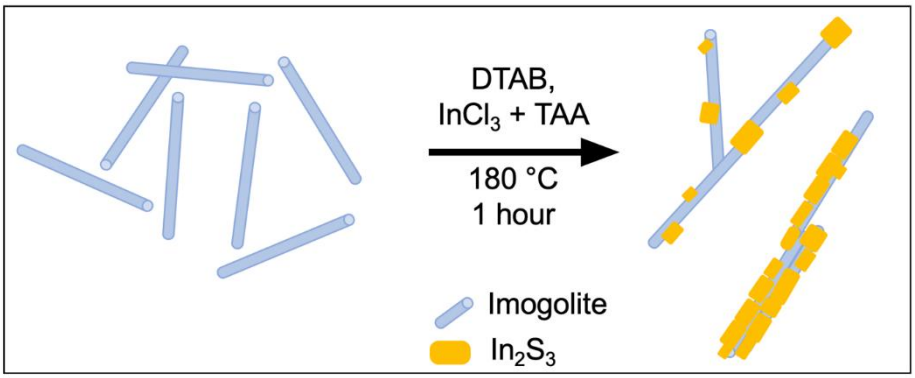

Scheme-1: Hydrothermal growth of In_2S_3 on imogolite nanotubes.

2.3. Characterization

Crystal structure of the samples was determined by X-ray diffraction (XRD) on a PANalytical X'PERT Pro diffractometer (Philips, Netherlands) using Cu Kα radiation (1.54 Å). Fourier transformed infrared (FTIR) spectra were measured on a Bruker Invenio R using golden gate ATR; 128 scans were averaged and recorded at a resolution of 4 cm^{-1}. A Cary 5000 UV-vis-NIR spectrometer (Agilent Inc., Santa Clara, CA, USA) was used for measuring diffuse reflectance UV-visible spectra of the samples with an integrating sphere. High-resolution transmission electron microscopy (HRTEM), high-angle annular dark field- scanning transmission electron microscopy (HAADF-STEM), and electron dispersive X-ray spectroscopy (EDX) mapping was performed on a Talos F200X (FEI, USA) equipped with 4 silicon drift EDX detectors.

2.4. Photocatalytic dye degradation

5 mg of the composite was added to a solution of methyl orange (15.25 µM, 20 mL), resulting in the final photocatalyst concentration of 0.25 mg/mL. This dispersion was illuminated with a 300 W Xe lamp (LSE340, LOT-Oriel GmbH & Co. KG, Germany) using a >400 nm long-pass filter (FEL0400, Thorlabs, Newton, NJ, USA) to remove UV light. Before illumination, the dye suspension was stirred for 30 mins to reach adsorption-desorption equilibrium. 1.5 mL aliquots were withdrawn at specific time points and centrifuged (4500rpm, 10 mins), after which the UV-vis absorbance spectra were recorded using a Cary 60 UV-vis spectrometer (Agilent Inc., Santa Clara, CA, USA). The same amount of INT was used in the control dye degradation experiments. For the In_2S_3 control experiments, an equivalent amount of In_2S_3 to that present in the composite was used (0.84 mg).

2.5 Photoelectrochemical Characterization

A Zahner Zennium XC electrochemical workstation was used for photoelectrochemical measurements. A three-electrode setup was used with an FTO photoanode, Ag/AgCl and platinum wire functioning as working, reference and counter electrodes, respectively. Chopped light voltammetry was carried out at an applied potential of 0V (vs Ag/AgCl) with light pulse period of 20s. Solar simulator (SS-F5-3A, Enli Tech Company, Taiwan) was used as the illumination source. Electrochemical impedance spectroscopy (EIS) was carried out with a sinusoidal AC perturbation of 10 mV applied over the frequency range of 0.1 to 1MHz. The samples were prepared by dispersing the powders (0.84 mg for IS and 5 mg for INT-IS_1h and INT) in 1.5 mL of PVA (10 mg/mL) and then drop casting 0.75 mL of the dispersion on the FTO substrate.

3. Results

XRD was performed in order to verify the effective growth of In_2S_3 and the presence of INT. The diffraction peaks from In_2S_3 cannot be observed in the composites, which implies the presence of scant amount of In_2S_3 in the composites (**Figure 1a**). Due to the finite radial dimensions of the nanotubes, the related diffractograms display large oscillations between 5 and 15° 2θ that are typical of the form factor of double-walled nanotubes. [27]In the case of composites, the signature of INTs is still present but the nanotubes undergo structural transformation after being exposed to hydrothermal conditions during the reactions. By the 3-hour time point, the appearance of additional peaks indicates the formation of another phase. In particular, the peak at 14.3° matches well with the (020) crystal plane of boehmite.[28,29] All the composites show the increase of a broad peak centered at 2θ ~62° with increasing reaction time, which can be ascribed to the (080) plane of boehmite.[28] Thus, from XRD it can be surmised that the hydrothermal transformation of INT to boehmite can be controlled by varying the reaction duration.

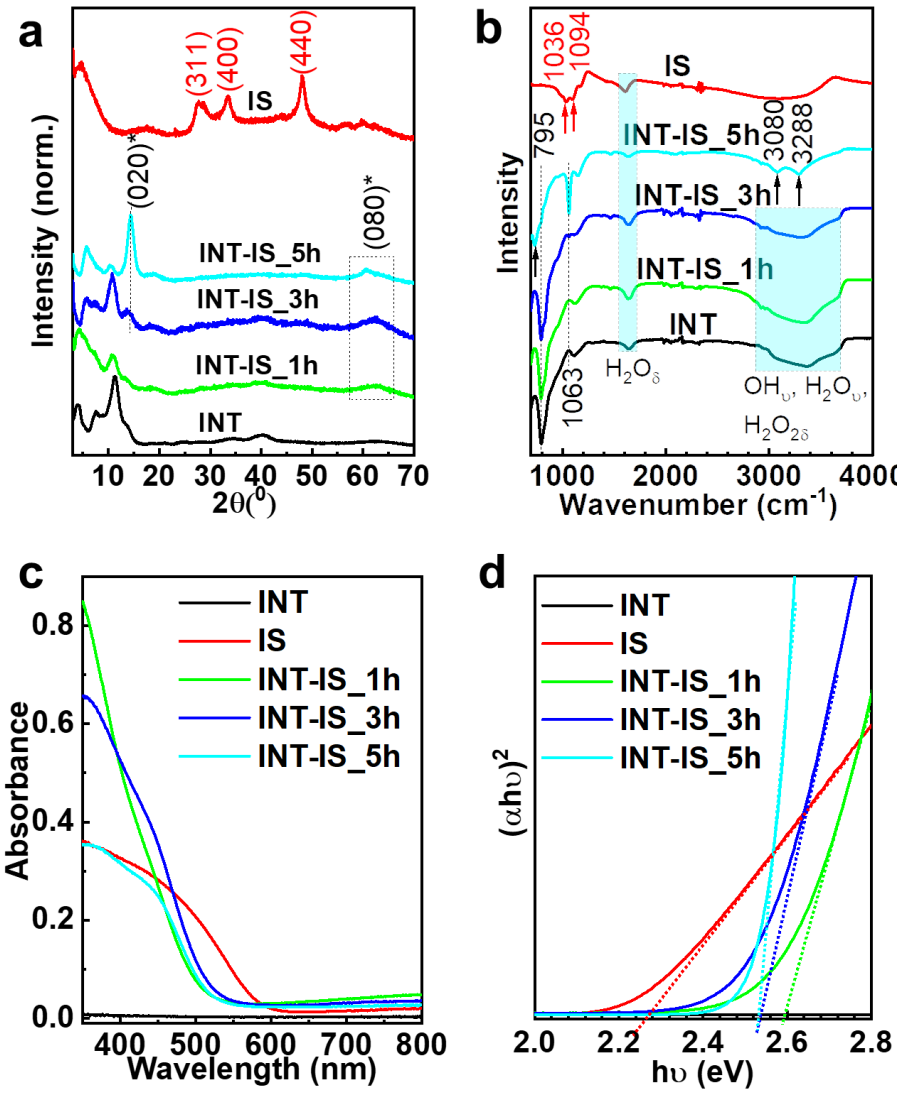

Figure 1. (a) X-ray diffractograms of the INT-In_2S_3 composites. *represents peaks belonging to boehmite (b) FT-IR spectra; (c) DRS UV-vis spectra of the INT-In_2S_3 composites. (d) Tauc plots of the INT-IS composites, dotted lines show the bandgap calculated by the Kubelka-Munk method.

These samples were further characterized by FTIR spectroscopy. The sharp peak at 795 cm^{-1} and the presence of a broad band between 2800 – 4000 cm^{-1} can be assigned to the Ge-O-Al stretch and to the υ stretching mode, bending mode of hydroxyl groups in water alongside the stretching vibrations of -OH groups belonging to INT, respectively (**Figure 1b**).[30,31] These bands are present in all the INT-IS composites except INT-IS_5h. The bands at 750, 1063, 1150, 3080 and 3288 cm^{-1} correspond to the torsional mode of Al-O, symmetric Al-O-H δ stretch, asymmetric Al-O-H δ stretch, symmetric Al-OH υ stretch and asymmetric Al-OH υ stretch, respectively. These bands indicate the formation of boehmite.[32] The 1063 cm^{-1} band is also present in the INT-IS_3h sample, however with diminished intensity compared to INT-

IS_5h. The bands in IS control seen at 1036 and 1094 cm^{-1} are due to the S-O stretch and υ stretch of CS present in the S source thioacetamide.[33,34] The absence of these bands in the composites indicates a relatively low amount of In_2S_3 present in these samples. Overall, FTIR characterization corroborates the observations from XRD.

The UV-vis-DRS spectra of the samples show that the light absorption in the composites is primarily due to the presence of In_2S_3, since INT has negligible absorption in the wavelength range measured (**Figure 1c**). Interestingly, the composites present a blue shift of the absorption band edge compared to the IS control, the largest blue-shift being observed in INT-IS_1h. This blue shift is plausibly due to the small size of In_2S_3 particles present in these composites (**Figure 2**).[35] The bandgap of the samples was calculated using the Kubelka-Munk method (**Figure 1d**).[36],[37] The bandgaps of IS, INT-IS_1h, INT-IS_3h and INT-IS_5h were founded to be 2.27, 2.59, 2.54 and 2.53 eV, respectively.

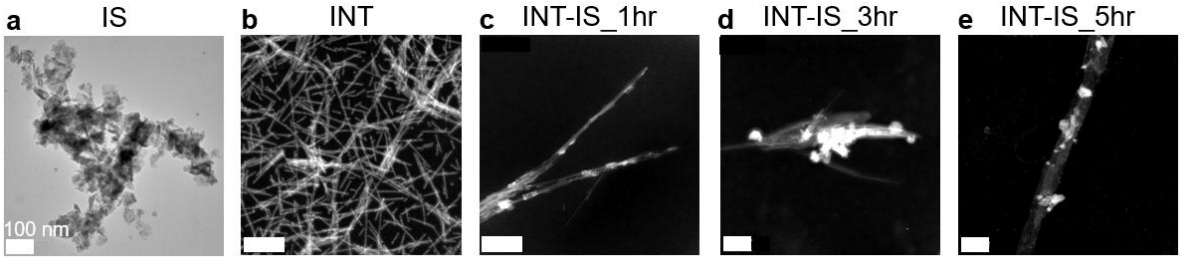

Figure 2. (a) Bright field TEM image of IS; HAADF-STEM images of (b) INT; (c) INT-IS_1h; (d) INT-IS_3h; (e) INT-IS_5h. All scale bars are 100 nm. Additional images of these samples are presented in the **Figure S1**.

Pristine IS forms irregularly-shaped sheets (**Figure 2a**), with a thickness of ~5 nm (**Figure S1**). The INT sample shows tubes having a diameter ~4.5 nm and an average length ~88 nm (**Figure 2b**), similar to those reported previously[21] In the case of the sample INT-IS_1h, the tubular morphology of INT is largely preserved, but the tubes seem to be linked together into bundles after In_2S_3 growth (**Figure 2c, Figure S1**). The brighter spots represent the In_2S_3, due to the increased atomic number of In relative to Ge and Al. In the presence of INT, In_2S_3 grows atop INT, however the reaction time drastically affects the morphology of the grown In_2S_3. Furthermore, as the reaction time is increased to 3 and 5 hours, the INT's tubular morphology is transformed into elongated sheets (**Figure 2d, e and S1**). The XRD and FTIR results suggest that this change in morphology is due to the transition from imogolite to boehmite at longer reaction times. The absence of isolated In_2S_3 particles in the hybrids

suggests that the surfactant modification of the INT surface as well as the In and S precursor concentrations chosen ensured the nucleation of In_2S_3 crystals on the INT.

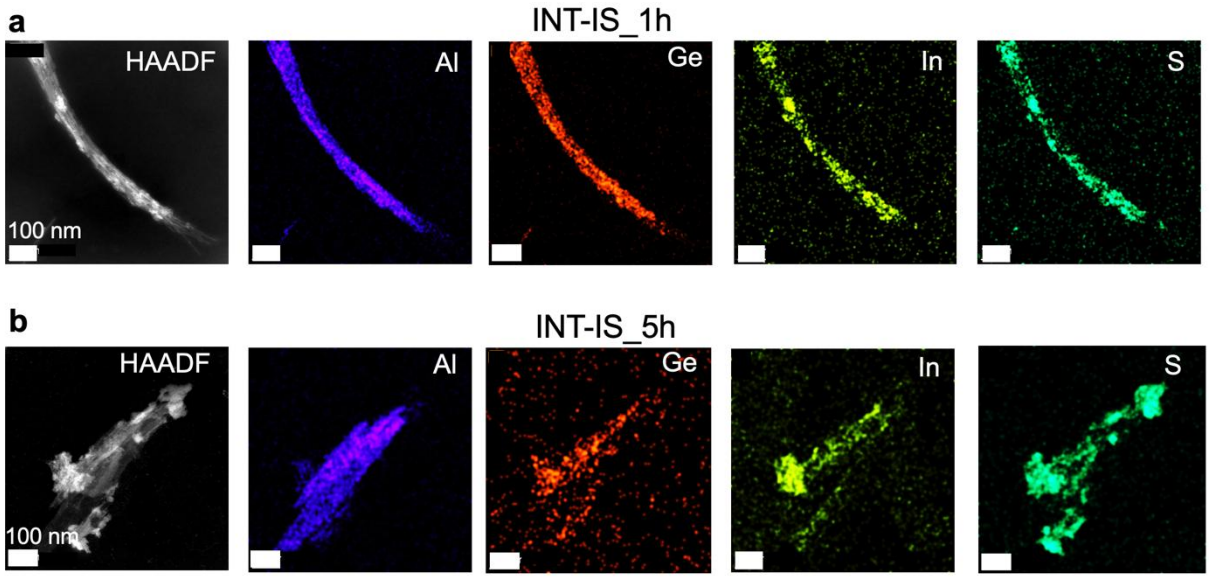

Figure 3. HAADF-STEM EDX mappings of (a) INT-IS_1h; (b) INT-IS_5h. EDX spectra of these mappings are presented in the **Figure S2**.

HAADF-STEM EDX mappings were performed on the samples for a closer examination of In_2S_3 growth on INT and state of INT after the hydrothermal reactions (**Figure 3**). In the case of the sample INT-IS_1h, the continuous growth of In_2S_3 along the tube axis was observed, in addition to the growth of separate In_2S_3 particles along the tube length (**Figure S1**). From the EDX spectra, it can be seen that peaks belonging to all the constituent elements are present for the sample INT-IS_1h (**Figure S2a**). However, for the sample INT-IS_5h, the characteristic peak of Ge (Kα and Lα) have almost disappeared, indicating the transformation of INT to boehmite (**Figure S2a**). From above mappings of the same sample, it can also be evidenced that after 5 hours the slender tubes seen in INT-IS_1h are transformed into elongated sheets, which signify the conversion of INT into boehmite.

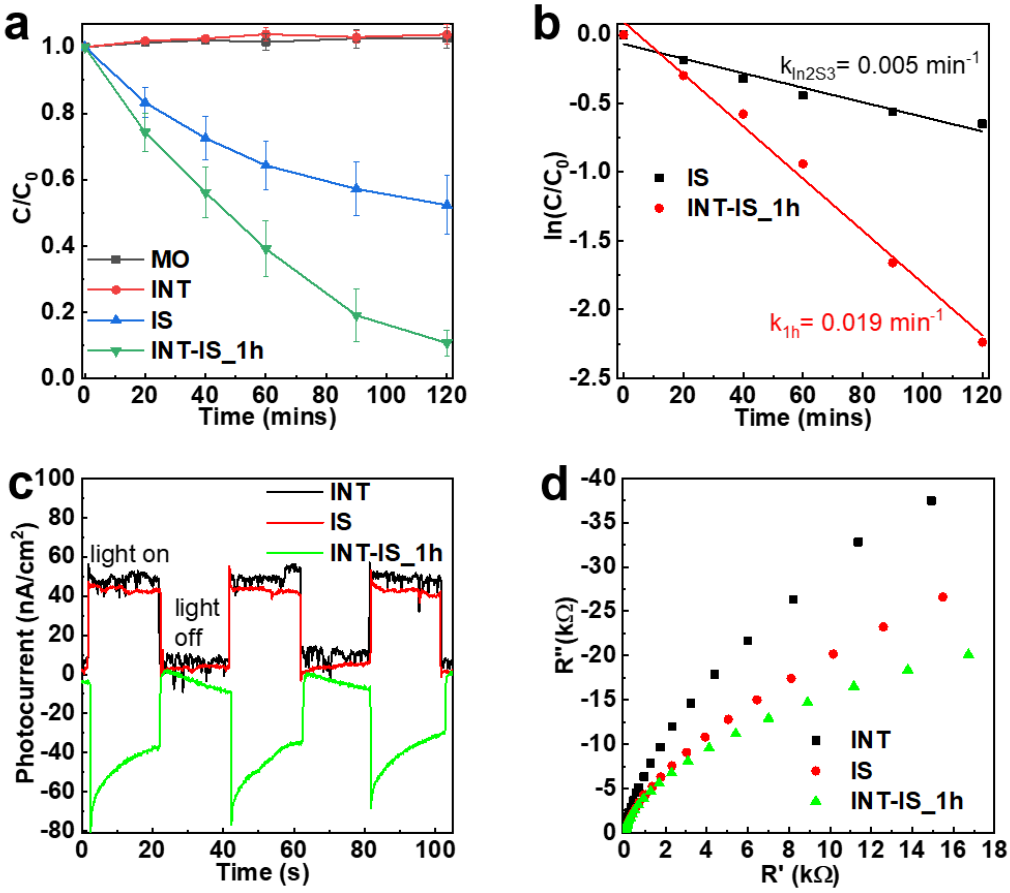

Figure 4. (a) Photocatalytic dye degradation of MO (corresponding UV-vis spectra are shown in **Figure S3**); (b) apparent first order rate constant for MO photodegradation, ([MO] = 15.25 µM, [particles] = 0.25 mg/mL); (c) Transient photocurrent response and (d) Nyquist plots of the composite and controls.

Photocatalytic performance of these composites was evaluated by photocatalytic degradation of the dye MO in visible light (>400 nm). MO is used as it does not photolyze upon illumination in the visible. INTs also afford no dye degradation under visible light illumination (**Figure 4a**). The photocatalytic degradation of MO by IS is significantly lower than that of INT-IS_1h. The former could degrade ~50% of the dye in 2 hours, whereas the latter, having the same amount of In_2S_3 as IS, degraded ~90% MO in the same time. The analysis of the dye degradation kinetics shows that the pseudo-first order rate constant is enhanced by almost four times for INT-IS_1h compared to the IS control (**Figure 4a**). Since [In_2S_3] was identical during the photocatalytic dye degradation with the samples INT-IS_1h and IS control, these results suggest that the introduction of INT induces a synergetic effect which enhances the photocatalytic activity of In_2S_3. It is to be noted that this improvement in photocatalysis occurs even with INT-IS_1h having a ~14% larger band gap than IS control.

Laponite-In_2S_3 composites reported by Liu et al also showed improved photocatalysis despite a drastically increased band gap.[13] Upon comparison, the INT-IS hybrids show a 19% increase in photocatalytic dye degradation rate compared to Laponite-In_2S_3 composites. Moreover, the INT-In_2S_3 composite after 1 hour of growth shows increased photocatalytic dye degradation compared with the boehmite-dominated sample synthesized with 5 hours of growth (**Figure S4a**). This suggests that the transformation of INT into boehmite is detrimental to the photocatalytic performance of the INT-IS hybrids. Also, the photocatalytic activity of INT-IS_1h decreased significantly after three reuse cycles, pointing to photodegradation of the hybrid during use (**Figure S4b**). While this may result from loss of particles during the recovery step, it may also result from the photodegradation of the INT interface. The photoactivity was further investigated using chopped light voltammetry with a solar simulator as the light source.

Samples INT and IS generate similar amount of photocurrent upon illumination (**Figure 4c**). It was noted that INT showed no photocatalytic activity upon illumination with only visible light, suggesting that INT is photoactive only in the UV region of the spectrum due to its low light absorption in the visible range (**Figure 1c**). INT and IS by themselves showed a typical positive photocurrent response, however, the composite INT-IS_1h displayed a negative photocurrent response. This points toward some effect of the interface between INT and IS which allows increased mobility of photogenerated holes. A similar negative photocurrent response was observed in the composites of reduced graphene oxide (RGO)-WS_2 by Rath et al.[38] They attributed this behavior to the p-type nature of RGO and the formation of diffusion barrier between the valence band of RGO and conduction band of WS_2. Since INT exhibits p-type characteristics,[39] it seems plausible that a similar mechanism might be operating in INT-IS_1h. Interfacial charge transfer resistance was examined by EIS. Since the radius of the arc corresponds to the resistance, it can be seen INT-IS_1h shows the lowest interfacial charge transfer resistance followed by IS and then INT. The low interfacial resistance might be one of the factors contributing toward enhancing the photocatalytic dye degradation performance of INT-IS_1h.

4. Conclusions

By optimizing the reaction conditions, the growth of In_2S_3 was templated by surfactant-modified INT. The morphology of In_2S_3 changed from anisotropic platelets to a mix of linear growths along the INT particles after 1 h of growth, to small particles along the INT/Boehmite structure at longer reaction times. These In_2S_3 decorated INT exhibited a

~400% enhancement in the photocatalytic dye degradation rate of MO over pristine In_2S_3, even though the bandgap was increased by 14% in the composite. Moreover, the p-type character of INT and the formation of the interface with In_2S_3 also engendered a negative photocurrent response not seen in the parent constituent materials themselves. The increased photocatalytic performance of the INT-IS can be attributed to the high mobility of photogenerated holes, which can then directly lead to oxidative reactions of MO. The present study revealed that just like the discoidal clay, Laponite, a tubular clay, imogolite can also template the growth of In_2S_3, enhancing the resulting photocatalytic properties. This work shows that such morphology-based templating approaches can be utilized in a more general sense, and will encourage further research into the composites of functional materials with clays in general, and imogolite in particular. While further systematic studies are required to elucidate the role of the interface in enhancing photocatalysis, previously reported clay-templated syntheses of photocatalysts such as Bi_2MoO_6,[40] BiOI,[41] $ZnIn_2S_4$,[42] and MoS_2[43] suggest that there is yet a rich landscape of imogolite-based nanohybrid photocatalysts left to explore.

Supporting Information

Supporting Information is available from the Wiley Online Library or from the author.

Acknowledgements

This research was funded by the German Academic Exchange Service (DAAD) from the funds of the German Federal Ministry of Education and Research, BMBF (57565165). E.H.H. is

supported by the Cluster of Excellence "Advanced Imaging of Matter" of the Deutsche Forschungsgemeinschaft (DFG) EXC 2056-project ID 390715994. This project has received financial support from the CNRS through the International Emerging Actions program (IEA00669, SECOWIN). We are grateful to the Central Division of Electron Microscopy (BEEM) of TUHH for providing access to an FEI Talos F200X. We thank Prof. Manfred Eich of the Institute of Optical and Electronic Materials of TUHH for providing the PEC setup and Dr. Fatemeh Ebrahimi for useful discussions. We thank the Weller/ Vossmeyer groups for providing access to a Cary 5000 UV-vis-NIR spectrometer.

Received: ((will be filled in by the editorial staff))
Revised: ((will be filled in by the editorial staff))
Published online: ((will be filled in by the editorial staff))

References:

[1] C. J. Vörösmarty, P. B. McIntyre, M. O. Gessner, D. Dudgeon, A. Prusevich, P. Green, S. Glidden, S. E. Bunn, C. A. Sullivan, C. R. Liermann, P. M. Davies, *Nature* **2010**, *467*, 555.

[2] H. S. Wheater, P. Gober, *Water Resour. Res.* **2015**, *51*, 5406.

[3] B. J. M. Chaúque, F. G. Brandão, M. B. Rott, *J. Environ. Chem. Eng.* **2022**, *10*.

[4] A. Ruiz-Aguirre, J. G. Villachica-Llamosas, M. I. Polo-López, A. Cabrera-Reina, G. Colón, J. Peral, S. Malato, *Energy* **2022**, *260*.

[5] S. Rengaraj, S. Venkataraj, C. W. Tai, Y. Kim, E. Repo, M. Sillanpää, *Langmuir* **2011**, *27*, 5534.

[6] Y. Liu, C. Chen, Y. He, Z. Zhang, M. Li, C. Li, X. B. Chen, Y. Han, Z. Shi, *Small* **2022**.

[7] X. Tang, S. Yi, Q. Yuan, Q. Shu, D. Han, L. Feng, *Sol. RRL* **2022**, *6*, 1.

[8] M. Murugalakshmi, G. Mamba, S. A. Ansari, V. Muthuraj, T. I. T. Nkambule, *Colloids Surfaces A Physicochem. Eng. Asp.* **2022**, *634*, 127969.

[9] H. Qiu, S. Fang, G. Huang, J. Bi, *Environ. Res.* **2020**, *190*, 110018.

[10] M. Q. Yang, B. Weng, Y. J. Xu, *Langmuir* **2013**, *29*, 10549.

[11] Z. Braiek, T. Roques-Carmes, I. Ben Assaker, M. Gannouni, P. Arnoux, S. Corbel, R. Chtourou, *J. Photochem. Photobiol. A Chem.* **2019**, *368*, 307.

[12] J. Tan, M. Yu, Z. Cai, X. Lou, J. Wang, Z. Li, *J. Colloid Interface Sci.* **2021**, *588*, 547.

[13] J. Liu, S. Jatav, E. H. Hill, *Chem. Mater.* **2020**, *32*, 10015.

[14] E. Paineau, *Appl. Sci.* **2018**, *8*.

[15] J. Govan, N. Arancibia-Miranda, M. Escudey, B. Bonelli, F. Tasca, *Mater. Chem. Front.* **2021**, *5*, 6779.

[16] L. Guimarães, A. N. Enyashin, J. Frenzel, T. Heine, H. A. Duarte, G. Seifert, *ACS Nano* **2007**, *1*, 362.

[17] G. Monet, M. S. Amara, S. Rouzière, E. Paineau, Z. Chai, J. D. Elliott, E. Poli, L. M. Liu, G. Teobaldi, P. Launois, *Nat. Commun.* **2018**, *9*.

[18] E. Paineau, G. Monet, V. Peyre, C. Goldmann, S. Rouzière, P. Launois, *Langmuir*

2019, *35*, 12451.

[19] G. I. Yucelen, D. Y. Kang, R. C. Guerrero-Ferreira, E. R. Wright, H. W. Beckham, S. Nair, *Nano Lett.* **2012**, *12*, 827.

[20] M. S. Amara, E. Paineau, S. Rouzière, B. Guiose, M. E. M. Krapf, O. Taché, P. Launois, A. Thill, *Chem. Mater.* **2015**, *27*, 1488.

[21] E. Paineau, S. Rouzière, G. Monet, C. C. Diogo, I. Morfin, P. Launois, *J. Colloid Interface Sci.* **2020**, *580*, 275.

[22] E. Paineau, M. E. M. Krapf, M. S. Amara, N. V. Matskova, I. Dozov, S. Rouzière, A. Thill, P. Launois, P. Davidson, *Nat. Commun.* **2016**, *7*, 1.

[23] S. Imamura, T. Kokubu, T. Yamashita, Y. Okamoto, K. Kajiwara, H. Kanai, *J. Catal.* **1996**, *160*, 137.

[24] W. J. Hsu, I. A. M. Ibrahim, Y. H. Lin, Z. H. Yang, G. I. Yucelen, J. W. Han, D. Y. Kang, *ACS Appl. Nano Mater.* **2019**, *2*, 6677.

[25] C. Hamon, E. Beaudoin, P. Launois, E. Paineau, *J. Phys. Chem. Lett.* **2021**, *12*, 5052.

[26] M. S. Amara, E. Paineau, M. Bacia-Verloop, M. E. M. Krapf, P. Davidson, L. Belloni, C. Levard, J. Rose, P. Launois, A. Thill, *Chem. Commun.* **2013**, *49*, 11284.

[27] G. Monet, S. Rouzière, D. Vantelon, C. Coelho Diogo, D. Maurin, J. L. Bantignies, P. Launois, E. Paineau, *J. Phys. Chem. C* **2021**, *125*, 12414.

[28] T. C. Alex, A. J. Kailath, R. Kumar, *Metall. Mater. Trans. B Process Metall. Mater. Process. Sci.* **2020**, *51*, 443.

[29] X. Zhang, P. L. Huestis, C. I. Pearce, J. Z. Hu, K. Page, L. M. Anovitz, A. B. Aleksandrov, M. P. Prange, S. Kerisit, M. E. Bowden, W. Cui, Z. Wang, N. R. Jaegers, T. R. Graham, M. Dembowski, H. W. Wang, J. Liu, A. T. N'Diaye, M. Bleuel, D. F. R. Mildner, T. M. Orlando, G. A. Kimmel, J. A. La Verne, S. B. Clark, K. M. Rosso, *ACS Appl. Nano Mater.* **2018**, *1*, 7115.

[30] G. Monet, E. Paineau, Z. Chai, M. S. Amara, A. Orecchini, M. Jimenéz-Ruiz, A. Ruiz-Caridad, L. Fine, S. Rouzière, L. M. Liu, G. Teobaldi, S. Rols, P. Launois, *Nanoscale Adv.* **2020**, *2*, 1869.

[31] E. Paineau, P. Launois, *Crystals* **2020**, *10*, 1.

[32] Z. Wang, J. Gong, J. Ma, J. Xu, *RSC Adv.* **2014**, *4*, 14708.

[33] R. R. Iyengar, D. N. Sathyanarayana, C. C. Patel, *J. Inorg. Nucl. Chem.* **1972**, *34*, 1088.

[34] N. Chaudhari, L. Mandal, O. Game, S. Warule, D. Phase, S. Jadkar, S. Ogale, *ACS Appl. Mater. Interfaces* **2015**, *7*, 17671.

[35] J. Ning, K. Men, G. Xiao, L. Zhao, L. Wang, B. Liu, B. Zou, *J. Colloid Interface Sci.*

2010, *347*, 172.
[36] P. Makuła, M. Pacia, W. Macyk, *J. Phys. Chem. Lett.* **2018**, *9*, 6814.
[37] D. Chen, Z. Liu, *ACS Sustain. Chem. Eng.* **2018**, *6*, 12328.
[38] S. Ratha, A. J. Simbeck, D. J. Late, S. K. Nayak, C. S. Rout, *Appl. Phys. Lett.* **2014**, *105*.
[39] J. Park, J. Lee, S. Chang, T. Park, B. Han, W. H. Jin, W. Yi, *Bull. Korean Chem. Soc.* **2008**, *29*, 1048.
[40] S. Jatav, J. Liu, M. Herber, E. H. Hill, *ACS Appl. Mater. Interfaces* **2021**, *13*, 18713.
[41] J. Liu, S. Jatav, P. Wessel, E. H. Hill, *J. Phys. Chem. C* **2022**, *126*, 4975.
[42] J. Liu, S. Jatav, M. Herber, E. H. Hill, *Langmuir* **2021**, *37*, 4727.
[43] S. Jatav, K. P. Furlan, J. Liu, E. H. Hill, *ACS Appl. Mater. Interfaces* **2020**, *12*, 19813.

Table of Contents

This work shows that the tubular clay imogolite can template the growth of In_2S_3, leading to improvement in photocatalytic performance over pristine In_2S_3 due to highly mobile photogenerated holes.

S. Jatav, H. Xiang, M. Herber, E. Paineau, and E. H. Hill**

Growth on Imogolite enhances the photocatalytic performance of In_2S_3

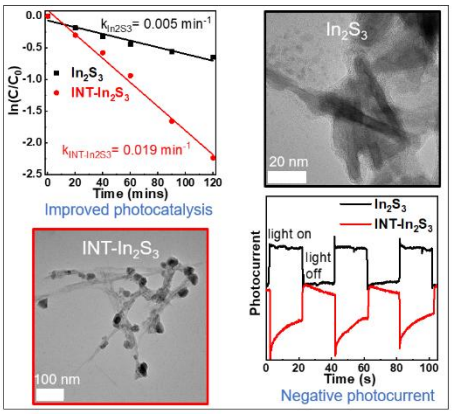

1

2

3

4